Letter | Editors' Suggestion

Magnetic structure of the topological semimetal $YbMnSb_2$

Jian-Rui Soh,[1] Siobhan M. Tobin,[2] Hao Su,[3] Ivica Zivkovic,[1] Bachir Ouladdiaf,[4] Anne Stunault,[4] J. Alberto Rodríguez-Velamazán,[4] Ketty Beauvois,[4] Yanfeng Guo,[3] and Andrew T. Boothroyd[2]

[1]*Institute of Physics, Ecole Polytechnique Fédérale de Lausanne (EPFL), CH-1015 Lausanne, Switzerland*
[2]*Department of Physics, University of Oxford, Clarendon Laboratory, Oxford OX1 3PU, United Kingdom*
[3]*School of Physical Science and Technology, ShanghaiTech University, Shanghai 201210, China*
[4]*Institut Laue-Langevin, 6 rue Jules Horowitz, BP 156, F-38042 Grenoble Cedex 9, France*

(Received 8 July 2021; accepted 10 September 2021; published 5 October 2021)

The antiferromagnetic (AFM) semimetal $YbMnSb_2$ has recently been identified as a candidate topological material, driven by time-reversal symmetry breaking. Depending on the ordered arrangement of Mn spins below the Néel temperature, $T_N = 345$ K, the electronic bands near the Fermi energy can either have a Dirac node, a Weyl node, or a nodal line. We have investigated the ground state magnetic structure of $YbMnSb_2$ using unpolarized and polarized single crystal neutron diffraction. We find that the Mn moments lie along the c axis of the $P4/nmm$ space group and are arranged in a C-type AFM structure, which implies the existence of gapped Dirac nodes near the Fermi level. The results highlight how different magnetic structures can critically affect the topological nature of fermions in semimetals.

DOI: 10.1103/PhysRevB.104.L161103

I. INTRODUCTION

Topological semimetals are materials whose electronic bands have a linear dispersion in the vicinity of the Fermi energy. Examples include crystals where the valence and conduction bands meet at discrete points (as in Dirac or Weyl semimetals) or along a one-dimensional curve in **k** space (in the case of nodal line semimetals) [1–3]. These systems can host electrons that mimic the behavior of massless fermions and are robust against perturbations due to the protection afforded by the topology of the electronic band structure [4,5].

The exploration of magnetic materials with a topologically nontrivial electronic band structure has become a central topic in quantum materials physics. A particular interest is to identify materials in which the topology of the electronic states can be controlled by their magnetic order [6–10]. Recently, the antiferromagnetic (AFM) metal $YbMnSb_2$ has been proposed as one such material, with the property that the topology of the bands near the Fermi energy (E_F) depends on the specific spin configuration on the Mn magnetic sublattice [11–16].

Previous studies have shown that the crystal structure of $YbMnSb_2$ can be described by the tetragonal space group $P4/nmm$ (No. 129) [11–13]. The unit cell, shown in Fig. 1(a), includes a square sublattice of Sb atoms which is predicted to host the topological fermions. This layer is in turn sandwiched between layers of Mn, facilitating the coupling between magnetism and electronic band topology. Depending on whether $YbMnSb_2$ displays G-type, C-type (with in-plane Mn moments), or canted C-type AFM order [see Figs. 1(b)–1(d)], the electronic bands are predicted to give rise to a nodal-line dispersion [13], a gapped Dirac crossing [12], or Weyl nodes [11], respectively. It is essential, therefore, to determine the magnetic order of the Mn sublattice in order to ascertain the topological nature of the fermions in $YbMnSb_2$.

In this Letter we determined the spin configuration of the Mn magnetic sublattice with high precision using a combination of polarized and unpolarized single crystal neutron diffraction. We find that below the Néel temperature the Mn spins point along the crystal c axis and are arranged in a C-type AFM structure [Fig. 1(e)]. The measurements place an upper limit of $0.01\mu_B$ on any in-plane ferromagnetic (FM) component (either above or below T_N). The particular C-type AFM structure found here is predicted to create gapped Dirac points in the calculated band structure of $YbMnSb_2$.

II. METHODS

Single crystalline samples of $YbMnSb_2$ were grown by the flux method, as described in Refs. [11,13], giving rise to shiny rectangular platelets with typical dimensions of $\sim 4 \times 4 \times 0.5$ mm^3. The structure and quality of the single crystals were checked on a six-circle x-ray diffractometer (Oxford Diffraction) and Laue diffractometer (Multiwire Laboratories).

Magnetization measurements were performed on a superconducting quantum interference device (SQUID) magnetometer (MPMS-3, Quantum Design) with magnetic field applied parallel and perpendicular to the crystal c axis. Measurements were performed in the temperature range $T = 2$–400 K and in fields of up to 3 T. Electrical transport measurements were performed on a physical property measurement system (PPMS, Quantum Design) with the resistivity option, in the temperature range 2–400 K in zero field.

Single crystal neutron diffraction with unpolarized neutrons of wavelength $\lambda = 2.36$ Å was performed on the four-circle diffractometer D10 at the Institut Laue-Langevin (ILL). The scattered neutrons were recorded on a 94×94 mm^2 area detector. To determine the magnetic and crystal

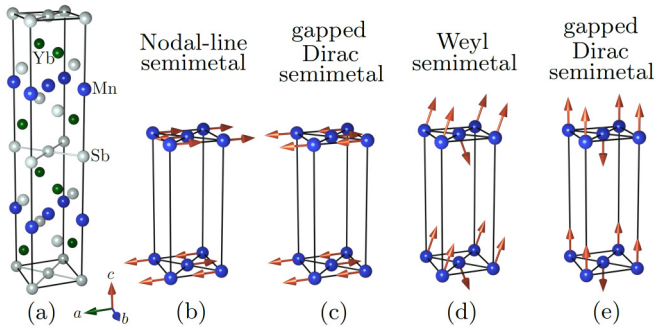

FIG. 1. (a) Two unit cells of $YbMnSb_2$ as described by the space group $P4/nmm$ with cell parameters $a = b = 4.31(2)$ Å, $c = 10.85(1)$ Å at $T = 400$ K. The square Sb layers (at $z = 0$ and c) are predicted to host different types of topological fermions, depending on the magnetic structure of the Mn magnetic sublattice. (b)–(e) show different Mn magnetic structures and the corresponding predicted topology of the electronic bands: (b) G-type AFM with in-plane Mn moments stabilizes a line node in the electronic bands; (c) C-type AFM with in-plane moments gives rise to Dirac nodes with a small gap; (d) a canted C-type AFM order gives rise to topologically protected Weyl nodes; (e) C-type AFM with moments along c stabilizes a gapped Dirac state.

structure of $YbMnSb_2$, a total of 382 and 386 hkl reflections were collected below and above the magnetic ordering temperatures, at $T = 2$ and 400 K, respectively [Fig. 3(a)]. To ascertain if there is a canting of the Mn moments away from the crystal c axis [Figs. 4(a) and 4(b)], the temperature dependence of several reflections was measured in the temperature range from 2 to 420 K.

Polarized neutron diffraction measurements ($\lambda = 0.832$ Å) were performed on the single-crystal diffractometer D3 (ILL) with a polarized incident beam but without a polarization analysis (half-polarized setup). The incident neutron polarization (P_i) was oriented either parallel or antiparallel to z (the normal to the scattering plane) by means of a cryoflipper, and maintained by guide fields. The crystal was aligned inside a vertical field superconducting magnet with the crystal b axis vertical to give access to a series of reflections in the $(h0l)$ horizontal scattering plane [Fig. 5(b)]. A magnetic field of $\mu_0 H = 0.4$ T was applied.

For both neutron diffraction experiments on the instruments D3 and D10, the single crystals were prealigned with the neutron Laue diffractometers OrientExpress [17] and CYCLOPS [18] at ILL. A neutron diffraction data analysis was performed with the MAG2POL software [19].

To clarify the topological nature of the electronic band structure in $YbMnSb_2$ we performed density functional theory (DFT) calculations of the electronic band structure using the QUANTUM ESPRESSO implementation [20]. Relativistic pseudopotentials were used in the calculations to account for the large spin-orbit coupling (SOC) arising from the heavy Sb ions which might lead to band inversion. Furthermore, a Hubbard $U = 4.1$ eV was used to model the strong electron-electron correlations due to the Mn $3d$ bands. The Mn spin configuration used in the calculations was obtained from the analysis of the neutron scattering data as input parameters. A Monkhorst-Pack **k**-point sampling mesh of $4 \times 4 \times 6$ was used [21].

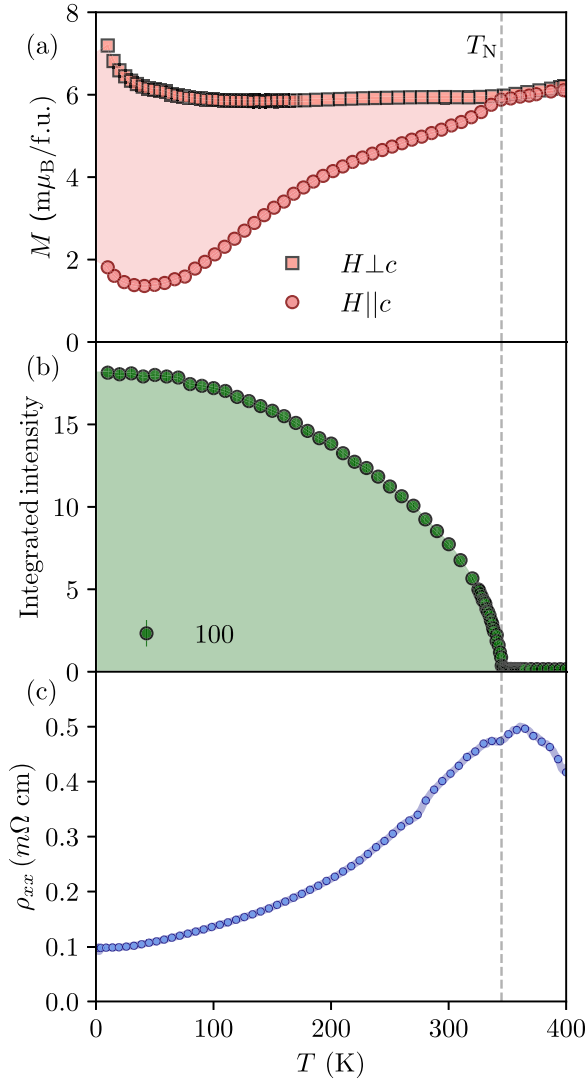

FIG. 2. (a) Temperature dependent magnetization curves of $YbMnSb_2$ measured with a field $\mu_0 H = 3$ T applied parallel and perpendicular to the crystal c axis. The bifurcation of the curves below $T_N = 345(1)$ K indicates the onset of AFM order. (b) Integrated intensity of the 100 magnetic reflection measured by neutron diffraction. (c) Temperature dependence of the in-plane resistivity of $YbMnSb_2$, displaying metallic conductivity for $T < T_N$.

III. RESULTS AND DISCUSSION

Figure 2(a) plots the magnetization of $YbMnSb_2$ as a function of temperature in a fixed field of $\mu_0 H = 3$ T, applied parallel and perpendicular to the crystal c axis. On cooling, we observe a bifurcation of the curves below $T_N = 345(1)$ K, indicating the onset of antiferromagnetic order of the Mn spins (the Yb atoms are divalent and therefore nonmagnetic). The anisotropy of the induced moment in the magnetically ordered phase, with $M_{\perp c} > M_{\| c}$, suggests that the crystal c axis is an easy axis. At low temperatures (below $T = 50$ K), we observe an upturn in the magnetization in both field configurations, consistent with an earlier report [11]. In a later section, we will discuss the possible origin of this behavior.

Figure 2(b) displays the temperature dependence of the integrated intensity of the 100 reflection measured by

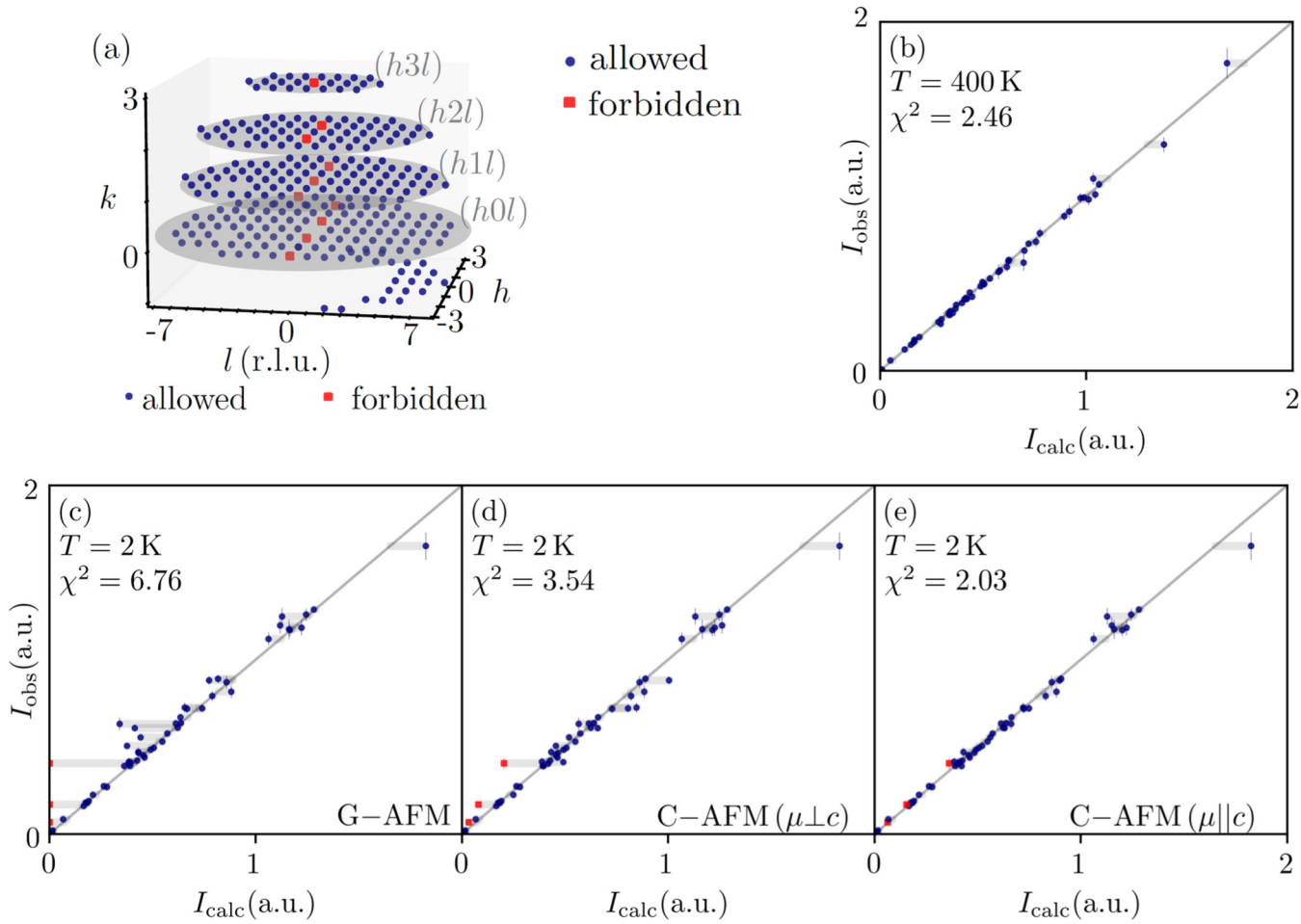

FIG. 3. (a) Reciprocal space representation of the *hkl* reflections that were measured on the D10 instrument. The blue and red points correspond to reflections which are allowed and forbidden, respectively, by the $P4/nmm$ space group. (b) Comparison of measured (I_{obs}) and calculated (I_{calc}) integrated intensities from the structural refinement in the paramagnetic phase of $YbMnSb_2$ at $T = 400$ K. (c)–(e) compare I_{obs} and I_{calc} for the $T = 2$ K data refined against structural models with *G*-type AFM, *C*-AFM (moments in plane), and *C*-AFM (moments along *c*), respectively.

neutron diffraction. The 100 reflection is structurally forbidden by the *n* glide, and its intensity has an order parameterlike dependence. Its appearance coincides with the bifurcation in the magnetic susceptibility at T_N. These observations confirm the existence of antiferromagnetism in $YbMnSb_2$.

In Fig. 2(c) we plot the in-plane longitudinal resistivity (ρ_{xx}) as a function of temperature. On cooling, we observe that ρ_{xx} increases to a maximum at T_N then decreases with temperature down to $T = 2$ K (the lowest temperature reached), in good agreement with earlier studies [11–13].

The broad resistivity peak in the vicinity of T_N could indicate a coupling between charge transport and fluctuations of the Mn moments, which diverge at T_N. *Ab initio* calculations of the electronic band structure of $YbMnSb_2$ demonstrate that the Sb square layer, which is structurally sandwiched between two Mn layers [Fig. 1(a)], is mainly responsible for charge transport [13]. Coupling between Mn $3d$ and Sb $5p$ states makes it possible for different Mn magnetic structures to cause different Sb $4p$ electronic topologies [see Figs. 1(b)–1(d)], and this is why it is important to understand the details of the AFM structure observed below T_N.

The magnetic structures depicted in Figs. 1(c)–1(e) can be described with a magnetic propagation vector $\mathbf{q} = (0, 0, 0)$. For $T < T_N$, therefore, magnetic Bragg peaks observed by neutron diffraction may coincide with structural Bragg peaks. Figure 3(a) illustrates the set of reflections measured in our diffraction study. These reflections are mostly structurally allowed in the $P4/nmm$ space group (indicated by the blue circles), but there are also a small number of reflections of the form $h + k = 2m + 1$ (m integer) which are forbidden by the *n* glide (red squares). The latter reflections, where present, are therefore purely magnetic in origin.

To identify the magnetic contribution to the structural Bragg peaks when $T < T_N$ it is important to obtain a good model for the crystal structure in the paramagnetic phase. Figure 3(b) shows the results of our refinement in the paramagnetic phase at $T = 400$ K. The observed and calculated peak intensities are seen to agree well. The refined structural parameters are given in Table I.

For completeness, we mention that we also observed some very weak nonmagnetic reflections at half-integer l positions which are structurally forbidden in $P4/nmm$ but allowed in the closely related *Pnma* space group. The latter space group was

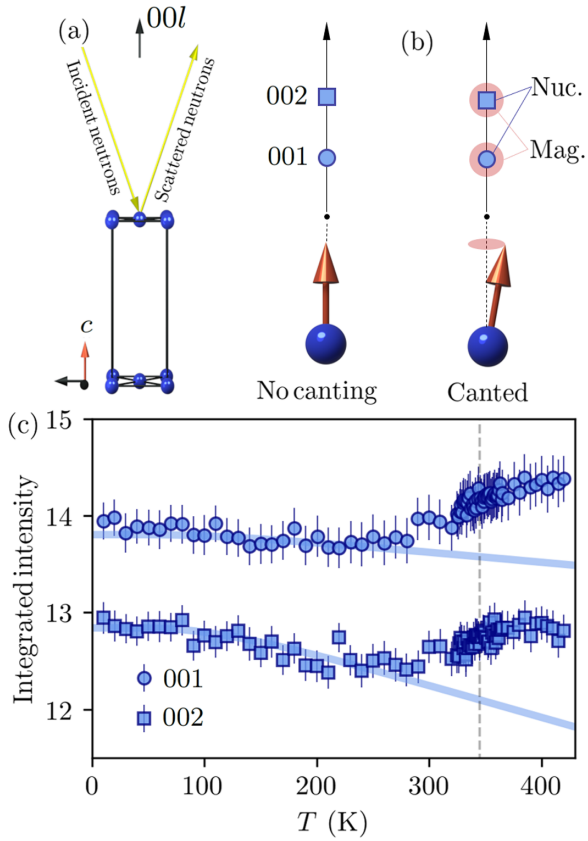

FIG. 4. (a) Unpolarized neutrons were used on the D10 instrument (ILL), with the scattering vector **Q** along 00l. (b) Since magnetic neutron diffraction is sensitive to the component of **M** perpendicular to **Q**, namely $\mathbf{M}_\perp$, a canting of the Mn moments away from the crystal c axis will produce a magnetic contribution to the nuclear Bragg reflections along 00l. (c) The temperature dependence of the integrated intensities of the 001 and the 002 reflections. The line corresponds to the fit to the Debye-Waller factor.

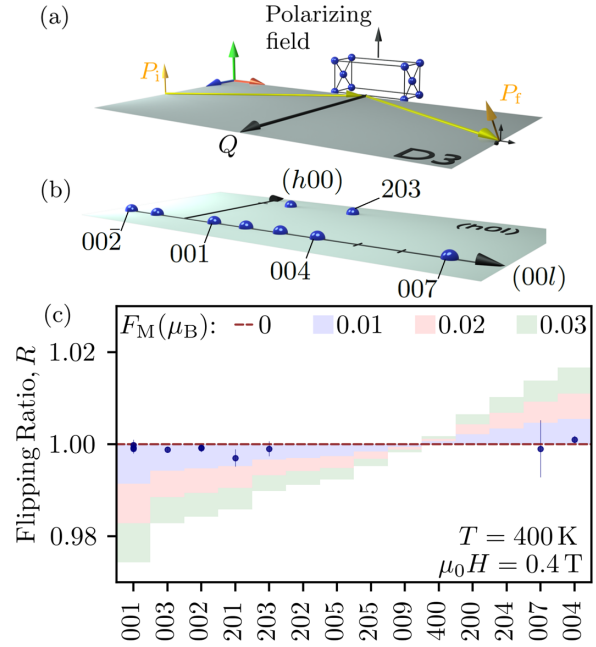

FIG. 5. (a) To access the ($h0l$) reflections in the half-polarized experimental setup on D3, a $YbMnSb_2$ single crystal was aligned with the crystal b axis normal to the horizontal scattering plane. The incident neutrons are polarized along z ($P_i \parallel z$) and the scattered neutron polarization P_f is not analyzed. (b) Reciprocal space plot of the measured reflections (blue spheres) in the ($h0l$) scattering plane. (c) Measured flipping ratios (blue circles) along with the calculated R for zero in-plane moment (dashed line) and several nonzero values up to $0.03\mu_B$ (colored bars).

reported to give an equally good description of x-ray diffraction data from polycrystalline $YbMnSb_2$ [11] and is known in the wider family of $AMnSb_2$ (A = Eu, Sr, Ca) compounds [22–27]. These half-integer reflections can arise from a subtle structural distortion which doubles the unit cell in the out-of-plane direction, but due to limited data we have not attempted to refine the structure further. The central conclusions of the study, which concern the magnetic structure, are not affected by the existence of such a distortion.

TABLE I. Structural parameters for $YbMnSb_2$ obtained from refinement in the space group $P4/nmm$ against integrated intensities collected at 400 K.

Atom	Wyckoff position	x	y	z	B_{iso}
Yb	2c	0.25	0.25	0.7274(1)	0.60
Mn	2a	0.75	0.25	0.00	0.4(1)
Sb	2b	0.75	0.25	0.50	0.78(7)
Sb	2c	0.25	0.25	0.1595(3)	0.49(8)

Turning to the 2 K data, we compare in Figs. 3(c)–3(e) the measured (I_{obs}) and predicted (I_{calc}) integrated intensities based on the magnetic structures shown in Figs. 1(b), 1(c), and 1(e). There are large discrepancies between I_{obs} and I_{calc} for the G-type AFM model, Fig. 3(b), especially for the purely magnetic reflections (red symbols) which have zero intensity for this magnetic structure. Hence, the G-type AFM order, shown in Fig. 1(b), can safely be excluded. Similarly, the I_{calc} values for the in-plane C-type AFM model significantly underestimate the intensities of the purely magnetic reflections [Fig. 3(c)]. Therefore, the in-plane C-type AFM model shown in Fig. 1(c) can also be excluded.

On the other hand, there is good agreement [see Fig. 3(d)] between the predicted and measured integrated intensities for the C-type AFM model with Mn moments along the crystal c axis, shown in Fig. 1(e). The size of the Mn moments obtained from the refinement is $3.48(9)\mu_B$, which is somewhat less than the value of $5\mu_B$ expected for divalent manganese with localized electrons ($3d^5$, $S = 5/2$), but consistent with the Mn ordered moments reported in related $AMnX_2$ intermetallic compounds (A = Ca, Sr, Ba, Yb; X = Sb, Bi) [25,28–31].

Let us now consider the structure shown in Fig. 1(d), which involves a canting of the C-type AFM structure so as to produce a net in-plane ferromagnetic (FM) moment. The possibility of a small FM canting was suggested by Wang *et al.* [11] to account for the upturn in the magnetization at low temperatures, and was reported in neutron scattering measurements on the sister compound $SrMnSb_2$ [25]. In

that study, Liu *et al.* observed an increase in the integrated intensities of the 200 reflection in the vicinity of T_N, and attributed the increase to an in-plane ferromagnetic order which sets in at $T_C \sim 565$ K (well above T_N). This in-plane ferromagnetic order in $SrMnSb_2$ is thought to persist into the AFM ordered phase below T_N, giving rise to the canted AFM order shown in Fig. 1(d).

To search for a small in-plane FM component we studied the temperature dependence of several $00l$ reflections. Magnetic neutron diffraction is caused by the component of the magnetic moment perpendicular to the scattering vector **Q**, so if the moments are aligned along the c axis then there is no magnetic contribution to any $00l$ reflections. On the other hand, any canting of the moments will produce a magnetic component perpendicular to c which will give magnetic scattering at $00l$ reflections. Figures 4(a) and 4(b) illustrate the arrangement just described.

Figure 4(c) plots the temperature dependence of the integrated intensities of the 001 and 002 reflections. At low temperatures (below $T = 50$ K), we do not observe an upturn in the integrated intensities which would indicate the onset of in-plane ferromagnetic order. Therefore, the increase in magnetic susceptibility at low temperatures, shown in Fig. 2(a), cannot be attributed to the development of a spontaneous ferromagnetic component in the crystal a-b plane. This conclusion is consistent with the behavior of the magnetization as a function of field at low T which also does not indicate spontaneous in-plane ferromagnetism (see Supplemental Material [32]). Instead, we attribute the upturn in the magnetic susceptibility at low temperatures to a very small concentration of a paramagnetic impurity, as reported in other members of the $AMnX_2$ family [29,33]. Hence, the canted AFM order, shown in Fig. 1(d), can be excluded at low temperatures.

However, we observed a gradual increase in the integrated intensity of the 001 and 002 reflections above $T \simeq 200$ K [Fig. 4(c)]. This increase, which is too large to be accounted for by paramagnetic diffuse scattering, could potentially arise from an in-plane ferromagnetic order of the Mn moments, giving rise to a canted magnetic structure [Fig. 1(d)] when $T < T_N$, as was reported in the neutron diffraction study of $SrMnSb_2$ [25]. To test for the presence of in-plane ferromagnetism in $YbMnSb_2$ we used polarized neutron diffraction to measure the flipping ratio (R) of a series of reflections within the ($h0l$) scattering plane at $T = 400$ K $> T_N$ [see Figs. 5(a) and 5(b)].

For centrosymmetric crystals and a magnetic field that is perpendicular to the scattering plane the flipping ratio is given by [34]

$$R = \left(\frac{1+\gamma}{1-\gamma}\right)^2 \simeq 1 + 4\gamma, \tag{1}$$

where $\gamma = F_M/F_N$ is the ratio of the magnetic to nuclear structure factor. The approximation is valid for $\gamma \ll 1$. When there is no magnetic contribution to the measured reflections ($F_M = 0$) the flipping ratio is seen from Eq. (1) to be $R = 1$. Conversely, a flipping ratio that deviates from unity implies a nonzero F_M. As the applied field was small ($\mu_0 H = 0.4$ T), the induced moment on paramagnetic Mn is negligible. Hence, if $R \neq 1$ we can infer a small FM contribution.

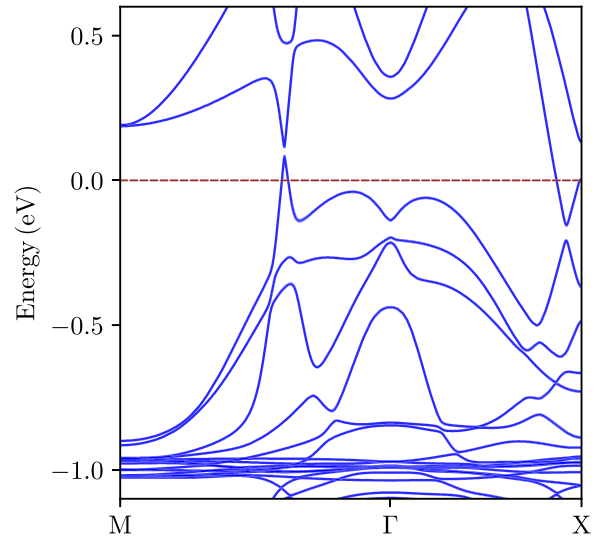

FIG. 6. *Ab initio* electronic dispersion of $YbMnSb_2$ along in-plane high symmetry directions. The calculation assumes the magnetic structure determined in this study.

Figure 5(c) plots flipping ratios measured at 400 K for the reflections that were studied. The plot also includes the calculated R for several values of the in-plane ferromagnetic moment up to $0.03\mu_B$. In particular, the dashed horizontal line denotes $R = 1$, which corresponds to zero ferromagnetic moment.

It can be seen from Fig. 5(c) that the measured R is consistent with an in-plane ferromagnetic component of less than $0.01\mu_B$. This is far too small to explain the observed increase in integrated intensity of the $00l$ reflections above $T \sim 200$ K, which we estimate would require an in-plane moment of about $0.8\mu_B$. Hence, the polarized neutron measurements exclude spontaneous in-plane magnetic order above $T \sim 200$ K. Furthermore, the magnetization as a function of field at $T = 400$ K also indicates that any in-plane ferromagnetic component is negligible ($M \lesssim 0.001\mu_B$) (see Supplemental Material [32]). A possible origin of the signal above $T \sim 200$ K [Fig. 4(c)] could arise from a MnSb impurity with ordering temperature of ~560 K [35].

The evidence presented here excludes all of the proposed magnetic structures presented in Figs. 1(b)–1(d) as acceptable models for the magnetic order of $YbMnSb_2$, and instead we find C-type AFM order with Mn moments along the crystal c axis [Fig. 1(e)]. We note that some of the predicted magnetic structures in Figs. 1(b)–1(d) were based on *ab initio* calculations, and the difference between the self-consistent energies obtained for the various magnetic structures can sometimes be of the same order of magnitude as the computational uncertainty. Hence, our work highlights the importance of identifying the ground state magnetic structure experimentally before proceeding to calculate the electronic band structure.

Finally, Fig. 6 shows the in-plane electronic dispersion of $YbMnSb_2$ calculated with the magnetic structure determined in this study. The band structure contains two avoided Dirac crossings close the Fermi energy, at $\Delta E \simeq -0.2$ eV along the Γ-X high symmetry line and $\Delta E \simeq 0.15$ eV between M and Γ. The gaps arise from the hybridization of the Sb $5p$ bands

[14,36]. The gapped Dirac dispersion of $YbMnSb_2$ is similar to that reported in other compounds exhibiting *C*-type AFM magnetic order in the $AMnSb_2$ family [26,28,37,38].

IV. CONCLUSION

In this Letter we experimentally tested several magnetic structures which have been predicted for $YbMnSb_2$. Magnetic structure refinements made from unpolarized neutron diffraction data provide conclusive evidence for *C*-type AFM order with Mn spins along the *c* axis. Polarized neutron diffraction measurements could not detect any in-plane FM order above or below T_N. The results do not support predictions that $YbMnSb_2$ is either a nodal line or a Weyl semimetal, and instead imply that the band structure contains gapped Dirac nodes near the Fermi level. More generally, this work highlights how different magnetic structures can profoundly affect the topological behavior of electrons in metals.

ACKNOWLEDGMENTS

The authors wish to thank H. Rønnow for helpful discussions, and D. Prabhakaran for assistance with sample preparation. The proposal numbers for the neutron scattering experiments on $YbMnSb_2$ are 5-41-1049 (D10), 5-53-305 (D3 [39]), EASY-671 (CYCLOPS) and EASY-667 (OrientExpress). Y-F.G. and A.T.B. acknowledge support from the Oxford–ShanghaiTech collaboration project. S.M.T. was supported by a scholarship from the Rhodes Trust. J.-R.S. acknowledges support from the Singapore National Science Scholarship, Agency for Science Technology and Research.

[1] S.-Y. Yang, H. Yang, E. Derunova, S. S. P. Parkin, B. Yan, and M. N. Ali, Adv. Phys.: X **3**, 1414631 (2018).
[2] C. Fang, H. Weng, X. Dai, and Z. Fang, Chin. Phys. B **25**, 117106 (2016).
[3] N. Kumar, S. N. Guin, K. Manna, C. Shekhar, and C. Felser, Chem. Rev. **121**, 2780 (2021).
[4] N. P. Armitage, E. J. Mele, and A. Vishwanath, Rev. Mod. Phys. **90**, 015001 (2018).
[5] N. Nagaosa, T. Morimoto, and Y. Tokura, Nat. Rev. Mater. **5**, 015001 (2020).
[6] Y. Xu, L. Elcoro, Z.-D. Song, B. J. Wieder, M. G. Vergniory, N. Regnault, Y. Chen, C. Felser, and B. A. Bernevig, Nature (London) **586**, 702 (2020).
[7] Z. Zhang, Z.-M. Yu, and S. A. Yang, Phys. Rev. B **103**, 115112 (2021).
[8] X. Gui, I. Pletikosic, H. Cao, H.-J. Tien, X. Xu, R. Zhong, G. Wang, T.-R. Chang, S. Jia, T. Valla, W. Xie, and R. J. Cava, ACS Cent. Sci. **5**, 900 (2019).
[9] L.-L. Wang, N. H. Jo, B. Kuthanazhi, Y. Wu, R. J. McQueeney, A. Kaminski, and P. C. Canfield, Phys. Rev. B **99**, 245147 (2019).
[10] J.-R. Soh, F. de Juan, M. G. Vergniory, N. B. M. Schröter, M. C. Rahn, D. Y. Yan, J. Jiang, M. Bristow, P. Reiss, J. N. Blandy, Y. F. Guo, Y. G. Shi, T. K. Kim, A. McCollam, S. H. Simon, Y. Chen, A. I. Coldea, and A. T. Boothroyd, Phys. Rev. B **100**, 201102(R) (2019).
[11] Y.-Y. Wang, S. Xu, L.-L. Sun, and T.-L. Xia, Phys. Rev. Mater. **2**, 021201(R) (2018).
[12] R. Kealhofer, S. Jang, S. M. Griffin, C. John, K. A. Benavides, S. Doyle, T. Helm, P. J. W. Moll, J. B. Neaton, J. Y. Chan, J. D. Denlinger, and J. G. Analytis, Phys. Rev. B **97**, 045109 (2018).
[13] Z. Qiu, C. Le, Z. Liao, B. Xu, R. Yang, J. Hu, Y. Dai, and X. Qiu, Phys. Rev. B **100**, 125136 (2019).
[14] S. Klemenz, S. Lei, and L. M. Schoop, Annu. Rev. Mater. Res. **49**, 185 (2019).
[15] S. Klemenz, A. K. Hay, S. M. L. Teicher, A. Topp, J. Cano, and L. M. Schoop, J. Am. Chem. Soc. **142**, 6350 (2020).
[16] Y. Pan, F.-R. Fan, X. Hong, B. He, C. Le, W. Schnelle, Y. He, K. Imasato, H. Borrmann, C. Hess, B. Bchner, Y. Sun, C. Fu, G. J. Snyder, and C. Felser, Adv. Mater. **33**, 2003168 (2021).
[17] B. Ouladdiaf, J. Archer, G. McIntyre, A. Hewat, D. Brau, and S. York, Phys. B: Condens. Matter **385–386**, 1052 (2006).
[18] B. Ouladdiaf, J. Archer, J. R. Allibon, P. Decarpentrie, M.-H. Lemée-Cailleau, J. Rodríguez-Carvajal, A. W. Hewat, S. York, D. Brau, and G. J. McIntyre, J. Appl. Crystallogr. **44**, 392 (2011).
[19] N. Qureshi, J. Appl. Crystallogr. **52**, 175 (2019).
[20] P. Giannozzi, S. Baroni, N. Bonini, M. Calandra, R. Car, C. Cavazzoni, D. Ceresoli, G. L. Chiarotti, M. Cococcioni, I. Dabo, A. D. Corso, S. de Gironcoli, S. Fabris, G. Fratesi, R. Gebauer, U. Gerstmann, C. Gougoussis, A. Kokalj, M. Lazzeri, L. Martin-Samos *et al.*, J. Phys.: Condens. Matter **21**, 395502 (2009).
[21] H. J. Monkhorst and J. D. Pack, Phys. Rev. B **13**, 5188 (1976).
[22] J.-R. Soh, P. Manuel, N. M. B. Schröter, C. J. Yi, F. Orlandi, Y. G. Shi, D. Prabhakaran, and A. T. Boothroyd, Phys. Rev. B **100**, 174406 (2019).
[23] D. Gong, S. Huang, F. Ye, X. Gui, J. Zhang, W. Xie, and R. Jin, Phys. Rev. B **101**, 224422 (2020).
[24] J. Liu, Quantum transport and magnetic properties of topological semimetals in $AMnSb_2$ (A = Sr, Ba, and Yb), Ph.D. thesis, Tulane University, 2017.
[25] J. Y. Liu, J. Hu, Q. Zhang, D. Graf, H. B. Cao, S. M. A. Radmanesh, D. J. Adams, Y. L. Zhu, G. F. Cheng, X. Liu, W. A. Phelan, J. Wei, M. Jaime, F. Balakirev, D. A. Tennant, J. F. DiTusa, I. Chiorescu, L. Spinu, and Z. Q. Mao, Nat. Mater. **16**, 905 (2017).
[26] J. B. He, Y. Fu, L. X. Zhao, H. Liang, D. Chen, Y. M. Leng, X. M. Wang, J. Li, S. Zhang, M. Q. Xue, C. H. Li, P. Zhang, Z. A. Ren, and G. F. Chen, Phys. Rev. B **95**, 045128 (2017).
[27] Q. Zhang, J. Liu, H. Cao, W. A. Phelan, J. F. DiTusa, D. A. Tennant, and Z. Mao, arXiv:2010.10405.
[28] J. Liu, J. Hu, H. Cao, Y. Zhu, A. Chuang, D. Graf, D. J. Adams, S. M. A. Radmanesh, L. Spinu, I. Chiorescu, and Z. Mao, Sci. Rep. **6**, 30525 (2016).
[29] Y. F. Guo, A. J. Princep, X. Zhang, P. Manuel, D. Khalyavin, I. I. Mazin, Y. G. Shi, and A. T. Boothroyd, Phys. Rev. B **90**, 075120 (2014).
[30] A. Wang, I. Zaliznyak, W. Ren, L. Wu, D. Graf, V. O. Garlea, J. B. Warren, E. Bozin, Y. Zhu, and C. Petrovic, Phys. Rev. B **94**, 165161 (2016).

[31] J. Y. Liu, J. Hu, D. Graf, T. Zou, M. Zhu, Y. Shi, S. Che, S. M. A. Radmanesh, C. N. Lau, L. Spinu, H. B. Cao, X. Ke, and Z. Q. Mao, Nat. Commun. **8**, 646 (2017).

[32] See Supplemental Material at http://link.aps.org/supplemental/10.1103/PhysRevB.104.L161103 for additional magnetization measurements, details of the structural refinement, and *ab initio* electron band calculations.

[33] J.-R. Soh, H. Jacobsen, B. Ouladdiaf, A. Ivanov, A. Piovano, T. Tejsner, Z. Feng, H. Wang, H. Su, Y. Guo, Y. Shi, and A. T. Boothroyd, Phys. Rev. B **100**, 144431 (2019).

[34] A. T. Boothroyd, *Principles of Neutron Scattering from Condensed Matter* (Oxford University Press, Oxford, U.K., 2020).

[35] Y. Liu, T. Ma, L. Zhou, W. E. Straszheim, F. Islam, B. A. Jensen, W. Tian, T. Heitmann, R. A. Rosenberg, J. M. Wilde, B. Li, A. Kreyssig, A. I. Goldman, B. G. Ueland, R. J. McQueeney, and D. Vaknin, Phys. Rev. B **99**, 054435 (2019).

[36] J. Park, G. Lee, F. Wolff-Fabris, Y. Y. Koh, M. J. Eom, Y. K. Kim, M. A. Farhan, Y. J. Jo, C. Kim, J. H. Shim, and J. S. Kim, Phys. Rev. Lett. **107**, 126402 (2011).

[37] S. V. Ramankutty, J. Henke, A. Schiphorst, R. Nutakki, S. Bron, G. Araizi-Kanoutas, S. K. Mishra, L. Li, Y. K. Huang, T. K. Kim, M. Hoesch, C. Schlueter, T. L. Lee, A. de Visser, Z. Zhong, J. van Wezel, E. van Heumen, and M. S. Golden, SciPost Phys. **4**, 010 (2018).

[38] S. Huang, J. Kim, W. A. Shelton, E. W. Plummer, and R. Jin, Proc. Nat. Acad. Sci. USA **114**, 6256 (2017).

[39] The neutron scattering data recorded on the D3 diffractometer at the Institut Laue-Langevin is available from https://doi.ill.fr/10.5291/ILL-DATA.5-53-305.